A Simulation of the Development of Successive Cells Along a Cold Outflow Boundary

ROBERT B. WILHELMSON AND CHING-SEN CHEN[1]

University of Illinois, Urbana 61801

(Manuscript received 3 August 1981, in final form 8 March 1982)

ABSTRACT

A three-dimensional numerical simulation is presented in which five new cells (clouds) develop in succession over a 4 h period. The cells that develop have common characteristics including a lifetime of ~40 min. They form at 30 min intervals in a convergent region along the cold outflow boundary that is established by previous cells. The propagation of the cloud system is several meters per second faster than individual cell movement due to the discrete development of new cells on the right flank of previous ones.

Analysis of the simulation indicates that the most pronounced changes near the surface are due to downdraft development. In contrast, there is only a weak signature of new updraft development near the surface in the convergence field. Each new updraft develops along the cold outflow boundary which moves slowly away from the previous cell. The air participating in the generation of a new cell appears to have originated 1–1.5 km below cloud base (2.6 km). As the cell grows and rain begins falling out of it, the updraft loses its roots in the subcloud layer and a new cell begins to form.

The sounding used to initialize the model was taken on a day that successive development occurred. Comparison of the observed and modeled cell behavior indicates some broad similarities, but also many differences. For example, new cell development was observed every 15 min. An explanation for this difference and the wide range of frequencies for new cell formation observed in other storms will require further study.

1. Introduction

Storms that produce severe weather have been broken down into types to obtain a better understanding of their evolution and structure. For example, in recent years the basic internal structure of the supercell has been more clearly delineated with the aid of Doppler radar and numerical models (e.g., Klemp *et al.*, 1981; Ray *et al.*, 1981). Considerable attention has also been directed toward gaining a better understanding of multicell storms in which the propagation of the storm is significantly affected by new cell growth. The distinction commonly made between the supercell and the multicell is that in the former, new updrafts which form along the cold outflow boundary feed the main updraft of the storm while in the latter they grow and remain separate entities. We recognize that the distinction between a new cell and an old one can sometimes be difficult, particularly when determined visually or through radar reflectivities; however, it is an important distinction for studying differences in the behavior of supercell and multicell storms and the relationship of this behavior to the environments in which they form. In this paper multicellular development characterized by successive new cell development along a cold outflow boundary will be investigated with the aid of a three-dimensional numerical storm model. The term "cell" is used in this modeling context to define a dynamic entity composed of an updraft and its associated downdraft (see Browning, 1977).

Multicellular development can occur in many forms. Therefore, in order to establish a context for discussion of the model simulation, several well-documented storms will be reviewed for which successive new cell growth is important to storm movement. The term "cell" in this observational context refers to regions of distinct high radar reflectivity which often are associated with an updraft–downdraft pair (i.e., the cell definition used when discussing model results). The different storms are summarized in terms of the frequency of new development, the lifetime of a cell, and the overall movement of the system in which the cells are an integral part. In a classic study, Browning and Ludlam (1960) found that the development of new cells affected the movement of the so-called Wokingham storm both before and after a period of quasi-steady behavior. On the basis of reflectivity data this development was idealized in the popular schematic shown in Fig. 1 (Browning, 1962). In the figure the small ovals represent cells in various stages of development. During part of the storm's lifetime at least six cells were identifiable as shown within the large ovals. Each cell (or row) could be identified from its predecessor for an hour or two due to the upshear development of

[1] Present affiliation: Department of Atmospheric Physics, National Central University. Chung-Li, Taiwan, 320, Republic of China.

0022-4928/82/071466-18$08.50

new towers within it, and it is interesting to note that the rate of formation of new cells appeared to be inversely proportional to their intensity, size and persistence. The occurrence of a large number of cells composed of one or more towers as schematized in Fig. 1 is not common to most well-documented multicell storms. Nevertheless, the relationship between cell and storm motion is frequently observed. The dashed 7 m s^{-1} vector in Fig. 2a illustrates the impact of discrete propagation on the overall storm motion as estimated from the data given by Browning and Ludlam (1960, Fig. 14). New cells that persisted formed at ~15 min intervals. This interval, coupled with the discrete propagation vector, means that new cells would appear on radar ~6 km south of the previous reflectivity center.

In another study, Marwitz (1972) investigated in detail the development of two Alberta hailstorms. In both cases discrete new cell development (in one case obtained through visual observation and by looking at reflectivities near the cloud-top level and in the other by studying cloud base PPI echo development) noticeably affected the direction of storm propagation as illustrated for the 16 July 1969 storm in Fig. 2b. However, the frequency of new development was somewhat irregular and cells persisted from ½ to greater than 1 h. In contrast, Chisholm (1973) studied another Alberta storm in which several new cells developed with radar lifetimes of about 24–30 min. There is very little time overlap between precipitation fields of separate cells near cloud top as shown in Fig. 3 and thus the period for new development is ~25 min. The discrete propagation vector is shown in Fig. 2c which, when coupled with the formation period, indicates that new reflectivities appear ~3.6 km to the south-southwest of old ones. Actually, the distance varies somewhat about this value (as seen in Fig. 3) because, in part, the reflectivities of decaying cells deviate toward the east from the cell motion vector shown in Fig. 2c.

The 25 min period for development of new cells is similar to that for the simulation to be discussed later. However, the more common period for new development in Alberta is closer to 10 min according to Chisholm and Renick (1972). They also noted that each cell is usually identifiable on radar for 20–30 min and that a total of 30 or more cells can develop in a similar fashion in one storm system. The implication of this behavior is that 2–4 distinct cells with typical lifetimes are visible on radar at any given time. The mean effect of discrete development on storm motion for the multicells they analyzed is shown in Fig. 2d. Although the discrete propagation vector is large for this case, new reflectivities occur ~4.3 km from the center of previous ones because of the short period for new development.

The effect of discrete propagation on storm motion has also been studied by Newton and Fankhauser

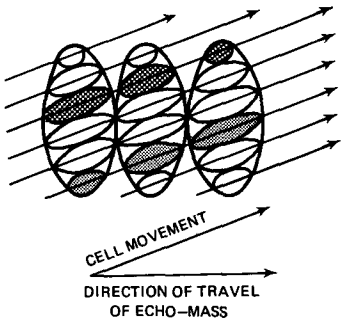

FIG. 1. A conceptual model of cell development during part of the Wokingham storm based on analysis of radar reflectivity patterns. New cells (small ovals) consisting of one or more towers develop systematically on the right flank of the echo mass (large ovals) as old ones decay on the left flank. (From Browning, 1962; Fig. 7.)

(1975) who documented new development to the south of a storm in Oklahoma as it proceeded in an eastward direction. In time these new cells appeared to move through the storm toward the north and dissipate. Due to new development the resulting storm speed toward the east was 5 m s^{-1} slower than the average individual cell speed and the resultant direction of propagation was further to the south as illustrated in Fig. 2e. The new development can be characterized by cells (or rows of towers) moving in the direction that individual towers within the cell moved as in Browning and Ludlam (1960). The new rows occur at irregular intervals and at any given time contain one to three reflectivity maxima. Further, the lifetimes of the rows range from 45 min to 3 h.

A different type of multicell storm has been documented by Fankhauser (1982) in which new cells formed in waves as a quasi-steady storm in Colorado collapsed. The development of groups of new cells to the south of old ones is responsible for the storm's approximate stationarity in the north-south direction in an environment in which a southerly wind component of at least 8 m s^{-1} was present at all levels below 8 km MSL (Potter sounding at 1450 MDT). Discrete development in this case cancels the effect of cell motion as shown in Fig. 2f with new cell development occurring to the rear of old cells rather than on the right flank (in terms of cell movement) as shown in previous panels. In contrast, new cells can also form to the front of old ones as illustrated by the behavior of another Colorado storm to be discussed later, but summarized here in Fig. 2g (Chalon *et al.*, 1976).

Analyses of not only the storms mentioned above but also many others indicate that discrete propagation can significantly affect storm motion, usually causing the storm as a whole to move to the right of individual cells as shown in Fig. 2. The simple depiction in this figure is meant as a guide to the

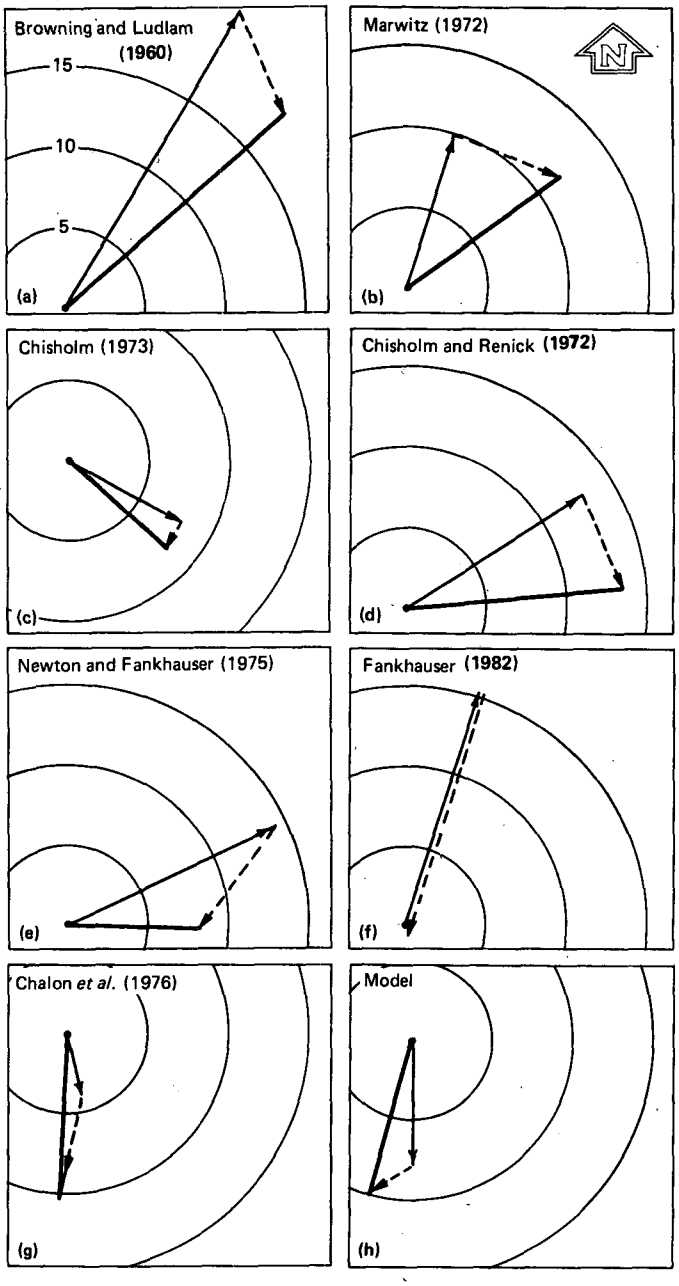

FIG. 2. Vectors showing the overall movement (thick solid) of a number of observed multicell storms [(a)–(g)] and of the modeled storm (h). The approximate movement of individual cells within these storms is also shown (thin solid vectors) and the effect of discrete propagation (dashed vectors) is indicated. The velocity circles are 5 m s^{-1} apart in all panels.

characteristic movement within different multicells. The observed development and movement can vary within a storm. New cells typically form ~4–10 km away from older ones. Thus, the magnitude of the discrete vector velocities (dashed) in Fig. 2 can be misleading if not linked to the frequency of new cell formation. In some of these storms a new cell forms as the previous one decays. This is illustrated in Fig. 3 where it is possible that enhanced convergence in the boundary layer due to the rain-induced downdraft of the previous cell acts to trigger a new cell. This hypothesis, however, does not appear to explain new cell development every 10–15 min, as it usually takes longer than this for a cloud to grow and produce surface precipitation. This is discussed further in Section 5.

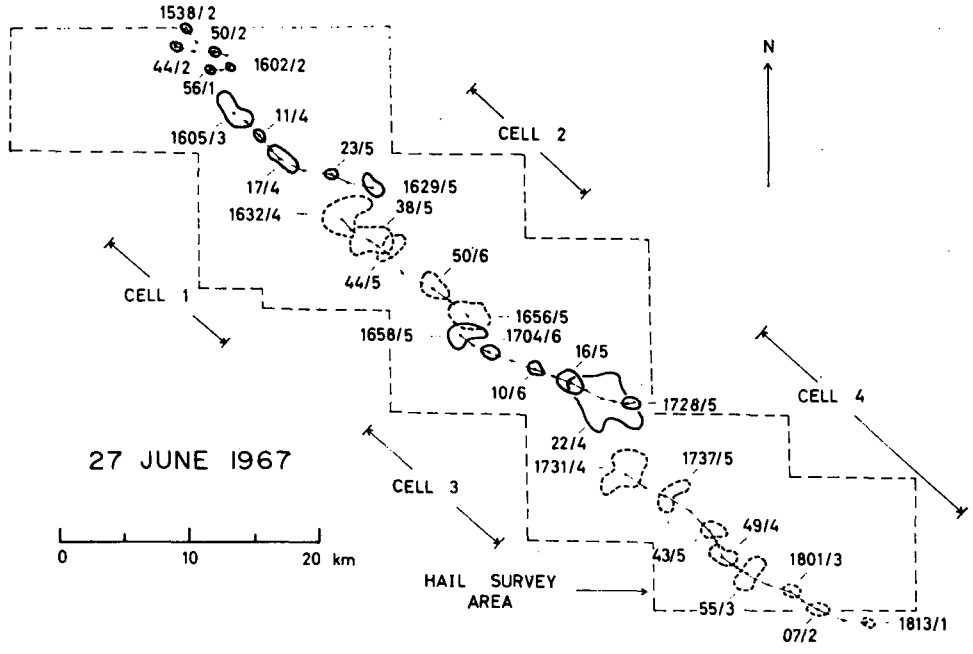

FIG. 3. Horizontal movement of the maximum radar storm top, 27 June 1967, at 3 min intervals (with echo configurations at 6 min intervals) for the period 1538–1813 MST. Times and elevation angles are indicated (e.g., 1538/2 denotes 1538 MST, 2° elevation). Note the formation of a new cell on the right-hand flank of the dissipating cell at 1632, 1658 and 1731. (From Chisholm, 1973; Fig. 46.)

The development of new cells associated with the decay of an initial one has been documented in several papers with the aid of three-dimensional models. Miller (1978) discussed a simulation of a multicellular storm in which several new cells formed in succession along the cold outflow boundary initially formed by a single precipitating cloud. The new cells were weaker than the original and developed in a region where the relative low winds opposing the spread of the outflow were strongest. It is not possible with the information given in the paper to determine the exact timing between new developments; however, the third cell appears to have formed ~15 min after the second. This is also the case in the multicell simulation reported by Thorpe and Miller (1978) in which the environmental wind profile was different from that used by Miller. In both papers the importance of cold outflow propagation away from the previous cells was underscored. This was contrasted with the behavior of a supercell storm in which the cold outflow stayed with the storm and continued to support its long-lived structure. In another paper, Tripoli and Cotton (1980) noted that the imposition of localized convergence changed the character of a cell which did not produce strong secondary development along its precipitation-induced outflow to one that did. This study along with a more recent one by Weisman and Klemp (1982) documents the importance of environmental conditions on a storm's subsequent development.

The simulation discussed in this paper is the outcome of the first successful effort to study multicell development with the Klemp-Wilhelmson storm model. Through modeling such storms we intend to investigate how their evolution is related to environmental conditions and how new cells form. The latter is emphasized in this paper. In the simulation new cell development is triggered by the decay of a single short-lived cloud in a horizontally homogeneous environment with moderate wind shear. Five new cells of similar intensity are produced in succession along the cold outflow boundary of previous cells. The simulation was made using the model reported by Klemp and Wilhelmson (1978a) with some alterations presented in Section 2. In Section 3 the simulation is discussed with emphasis on the overall development, on the changes below cloud base during the lifetime of a cell, and on the changes at the time of new cell formation. In the next section the simulation results are compared against the characteristics of multicell development on the day the sounding used to initialize the model was taken. Finally, additional discussion on the formation of new cells is presented in the summary.

2. The storm model

The three-dimensional numerical model used to study the triggering of new cells along a cold outflow boundary is based on the one given by Klemp and

Wilhelmson (1978a). This model utilizes the compressible equations which are efficiently solved by separating out sound wave terms and integrating them with a smaller time step than that used for the convective processes in order to maintain computational stability. The predicted variables include horizontal and vertical velocities, pressure, potential temperature, mixing ratios of water vapor, of cloud water and of rainwater, and subgrid mixing coefficient. The latter variable is computed with the aid of a prognostic turbulence energy equation that includes the influence of local shear, buoyancy and dissipation. Cloud water and rainwater growth are parameterized in the manner suggested by Kessler (1969), but with the coefficients used by Klemp and Wilhelmson. Several modifications made to the model are briefly discussed in this section and are more fully documented in the Appendix.

The cold outflow generated by a storm is usually concentrated in the lower 1–2 km of the atmosphere. In order to resolve the vertical characteristics of this outflow we decided to increase the vertical resolution in this region. The constant vertical grid interval used by Klemp and Wilhelmson could have been reduced, but this would have led to a significant increase in the number of grid points in the vertical and thus a significant increase in required computer resources. Instead, a vertically stretched grid was introduced in the numerical model through a transformation. The transformation and the resulting model equations are described in the Appendix. For the simulation to be discussed the vertical resolution ranged from 100 to 400 m below cloud base and from 400 to 900 m above. The horizontal grid spacing was held constant at 1.5 km in both horizontal directions. In addition, the large time step was 10 s and the small one was 2.5 s.

The horizontal grid spacing is at least twice the vertical spacing throughout most of the model domain. Klemp and Wilhelmson (1978a) used a fourth-order approximation (when linearized) for horizontal advection in order that the accuracy of horizontal advection be comparable to that obtained using a second-order approximation with a smaller vertical grid interval. However, their advective scheme is not conservative. For example, there is no guarantee that the total mass of water vapor would be conserved apart from changes in state or vapor flux through the model boundaries. In order to help guarantee conservation the equations for velocities and for mixing ratios of water vapor, cloud water and rainwater were finite-differenced in flux form using fourth-order approximations for the nonlinear horizontal fluxes. The resulting equations and further discussion are given in the Appendix.

The parameterization of the subgrid-scale processes in the model is basically the same as that used by Klemp and Wilhelmson (1978a). Closure is accomplished using mixing length theory on conservative variables with mixing coefficients defined in terms of the subgrid kinetic energy. Changes in the subgrid-scale energy are described by a prognostic equation in which advection, shear, buoyancy, diffusion and dissipation effects are included. When the local Richardson number is small or negative, energy is generated. In the cloud model this means that significant energy and mixing occur within cloud updrafts and in almost neutral boundary layers with significant shear. Using the initial conditions to be presented, mixing does occur in the boundary layer where the base state Richardson number is positive but almost zero. The result of this mixing is a significant increase in moisture near the top of the boundary layer. In order to prevent this from happening the contribution of the base state to the generation of subgrid kinetic energy has been neglected.

The earlier parameterization is also altered to account for the vertically stretched grid. The mixing coefficient (K_m) is related to the subgrid energy (E) by the expression $K_m = C_m E^{1/2} l$ where C_m is a nondimensional constant and $l = (\Delta x \Delta y \Delta z)^{1/3}$ is the subgrid mixing length. In the expression for l, Δz is the actual grid size and not the constant transformed grid interval $\Delta z'$ (see the Appendix). The coefficient C_m is changed to 0.12 and the dissipation coefficient C_ϵ to 0.7. These numbers were suggested by Deardorff (1975, personal communication) for neutral and unstable situations and give somewhat less mixing than the 0.2 values used by Klemp and Wilhelmson. Further, the ratio of the mixing coefficient for heat and moisture (K_h) to the eddy mixing coefficient for momentum (K_m) is changed from 3 to 1. The latter change in subgrid mixing was made because some of our earlier simulations produced strong gust front convergence but no new clouds and it appeared that excessive mixing of scalar fields was preventing new growth.

Fourth-order horizontal damping with a coefficient $K_4 = 2.5 \times 10^9$ m^4 s^{-1} is used to discourage growth of nonlinear instability and to filter out very short wavelength modes which are likely of spurious origin. A second-order spatial filter of the form $K_2 A_{xx}$ is applied in the vertical to perturbations from the initial state (A) for the same reason at all but the lower and upper grid points and in all but the pressure equation with $K_2 = 100$ m^2 s^{-1}.

At the first level of the model the effect of surface drag is introduced by introducing the relation

$$V_t = C_D \frac{(u^2 + v^2)^{1/2}}{\Delta z} V,$$

where V is either u or v at the first level depending on the equation being solved and $\Delta z = 100$ m. A drag coefficient C_D of 0.02 is used based on the results of Mitchell and Hovermale (1977). The surface drag

is only allowed to affect perturbations of the velocities from those used to initialize the model; otherwise, the drag formulation would in time alter the base state environmental values. In a similar way the Coriolis force is also applied to perturbation velocities ($f = 0.0001\ s^{-1}$).

The lateral boundary condition approximation is modified so that the extrapolation scheme during outflow conditions depends on a variable "phase velocity" rather than a constant one as used by Klemp and Wilhelmson (1978a). This velocity is computed from the normal velocity equation at the boundary with a modified version of the technique studied by Orlanski (1976) and presented in the Appendix. It is difficult to argue whether this leads to a significant improvement in cloud simulation results over the approach used by Klemp and Wilhelmson, particularly for long simulations such as those to be presented. The reason for this is that increasing the model domain to significantly reduce boundary effects while retaining the same grid resolution is computationally unreasonable at this time. Simulations using the two approaches indicate that the boundary conditions have a noticeable effect on long-term simulations. However, it is encouraging that both approaches lead to similar qualitative results having similar interpretations.

3. A simulation of organized multicellular development

Wilhelmson and Klemp (1978) and Klemp and Wilhelmson (1978b) have used their numerical storm model to successfully simulate long-lived supercell storms. They found that such storms occurred as observed when the low to midlevel wind shear was strong. When weaker shear was used to initiate the model the initial convective cell decayed and only weak secondary convection developed along the outflow boundary. In order to pursue our study of secondary convective development we decided to use sounding data representative of the environment of an observed and well-documented multicell storm in which new cell development played a significant role in the overall storm propagation.

a. Model initialization

We chose to use initial data associated with a multicellular storm which developed in Colorado on 9 July 1973 during the National Hail Research Experiment. Analysis of this storm by Chalon *et al.* (1976) indicates that the observed periodic development of new cells may have been related to the downdraft production by preceding cells during their intense and decaying stages. Some details of this development will be discussed in Section 4 where they are compared to the simulation reported in this section. The sounding chosen for use in the model simulations was taken at Sterling (STK), Colorado. Chalon *et al.* (1976) considered this sounding to be reasonably representative of the storm's environment, although Sterling was ~40 km to the southeast of the storm area. The thermodynamic profile is reproduced in Fig. 4a using a skew-T diagram. The pseudo-adiabat having $\theta_e = 345.5$ K indicates moist ascent from cloud base where conditions were determined from the Queen Air aircraft data. The moisture content between 850 and 600 hPa (dotted line) was increased before using the sounding in the model. This modification was made in order to obtain a storm cell from an initial thermal bubble embedded in a horizontally homogeneous environment and is plausible based on mixing ratios reported by aircraft near the storm during the time of interest (Musil *et al.*, 1976).

The smoothed wind hodograph from STK used in initializing the model is shown in Fig. 4b. The low-level winds are from the northeast, midlevel winds from the north and upper level winds from the west. In some 1 km intervals the vector shear is greater than 5 m s^{-1} km^{-1}, but below 9 km MSL these layers are separated by ones of weaker shear. The overall vector shear is ~2.2 m s^{-1} km^{-1}, which is similar to environments of both single and multicell storms according to characteristics of the environments of these storms as synthesized by Fankhauser and Mohr (1977). The overall shear was computed using the average wind speed and height from the lifted condensation level (~4 km) to the unmixed parcel equilibrium level (~12 km) and from the average surface winds in the lowest 50 mb (approximately represented by the 2 km vector).

The simulation domain was moved with the cloud development over the 4 h integration to insure that the cloud activity remained near the center of the domain. In the simulation discussed in this section this was accomplished initially by adding 3 and 5 m s^{-1} to u and v, respectively. At 1.5 h, 4 m s^{-1} was added to v while at 2 h an additional 2 m s^{-1} was added. At 3 h, 1 m s^{-1} was subtracted from u while later at 3.5 h, 1 m s^{-1} was subtracted from v. These changes were made instantaneously and the errors associated with them are considered to be small based on several numerical tests. The drag and Coriolis force computations were unaffected by these changes as they were based on the observed winds.

The initial cloud was triggered by a thermal impulse in the form of a localized heat source that was applied over a 3 min period. It was horizontally centered at $x = 30.7$ km, $y = 38.2$ km within the 60 km × 60 km × 13 km domain and vertically specified at 702, 906 and 1222 m, three levels well below cloud base (2.6 km AGL). At each level a heating rate of 0.3 K min^{-1} was applied at four neighboring grid points and 0.2 K min^{-1} at the twelve surrounding

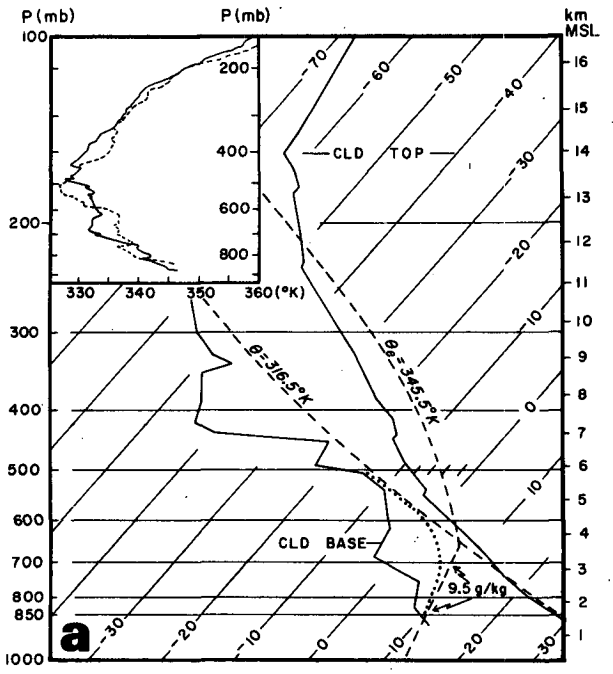

FIG. 4a. A skew-T diagram showing the temperature and dew point from the 1630 STK sounding on 9 July 1973. Labeled dashed curves designate dry and moist adiabats and mixing ratio representative of measured cloud base conditions. The dotted line describes the moisture profile used in the model simulation. The inset shows θ_e [K] vs pressure (mb) for STK 1630 (solid) and GRO 1735 (dashed) soundings. (Adapted from Chalon *et al.*, 1976; Fig. 3.)

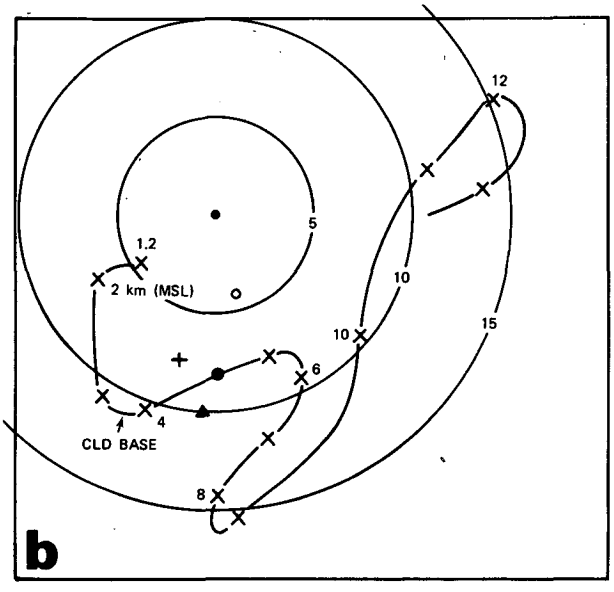

FIG. 4b. The smoothed hodograph used in the model simulation based on the 1630 STK sounding. The open and closed circles indicate the speed of the observed and modeled cells, respectively. The plus mark indicates the average of the 2–6.5 km wind vectors while the triangle indicates the average of the 2–9.5 km vectors.

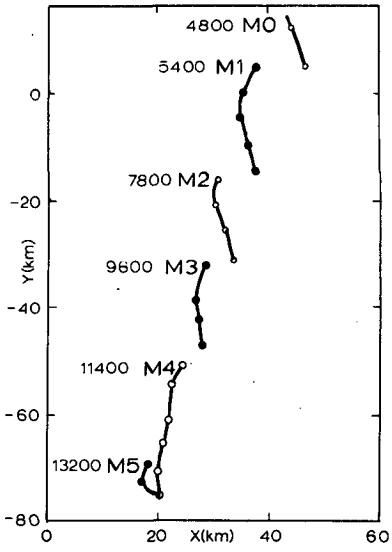

FIG. 5. The horizontal movement of the six simulated cells, M0–M5, from 4800 to 14 400 s. The dots indicate the location of the rain maximum at 10 min intervals near the cloud base (3.8 km MSL or 2.6 km AGL).

ones. The impact of this type of impulse on subsequent development in comparison to that used by Klemp and Wilhelmson (1978a) is discussed by Chen (1980).

b. An overview of the simulation

In response to the initial heating, a cloud (M0) grows and produces precipitation which reaches the ground around 3600 s. The associated cold outflow and low-level convergence ring spreads out in all directions relative to the cloud, and to the southwest triggers a new cell (M1) as shown in Fig. 5. In this figure the horizontal position of M0, M1, and subsequent cells are represented by dots at 10 min intervals. The dots indicate the location of the maximum rainwater content at cloud base for each cell (~2.6 km AGL) in the observational framework and are connected by a solid line. The times at which new cells occur are indicated in seconds while the axes are labeled so that the location of M1 is roughly the same as the observed cell W1 to be discussed later. After rain formation M1 moves to the south and eventually disappears as another new cell (M2) appears. In a similar fashion M3 appears as M2 dies and M4 appears as M3 dies. Finally, M5 appears and then merges with M4 as indicated by the half-solid, half-open dot. Shortly after this time a cell started to grow near the western boundary of the domain, apparently due to artificial boundary effects and thus the simulation was terminated.

It is apparent from Fig. 5 that each new cell appears ~30 min after the preceding one. Further, the

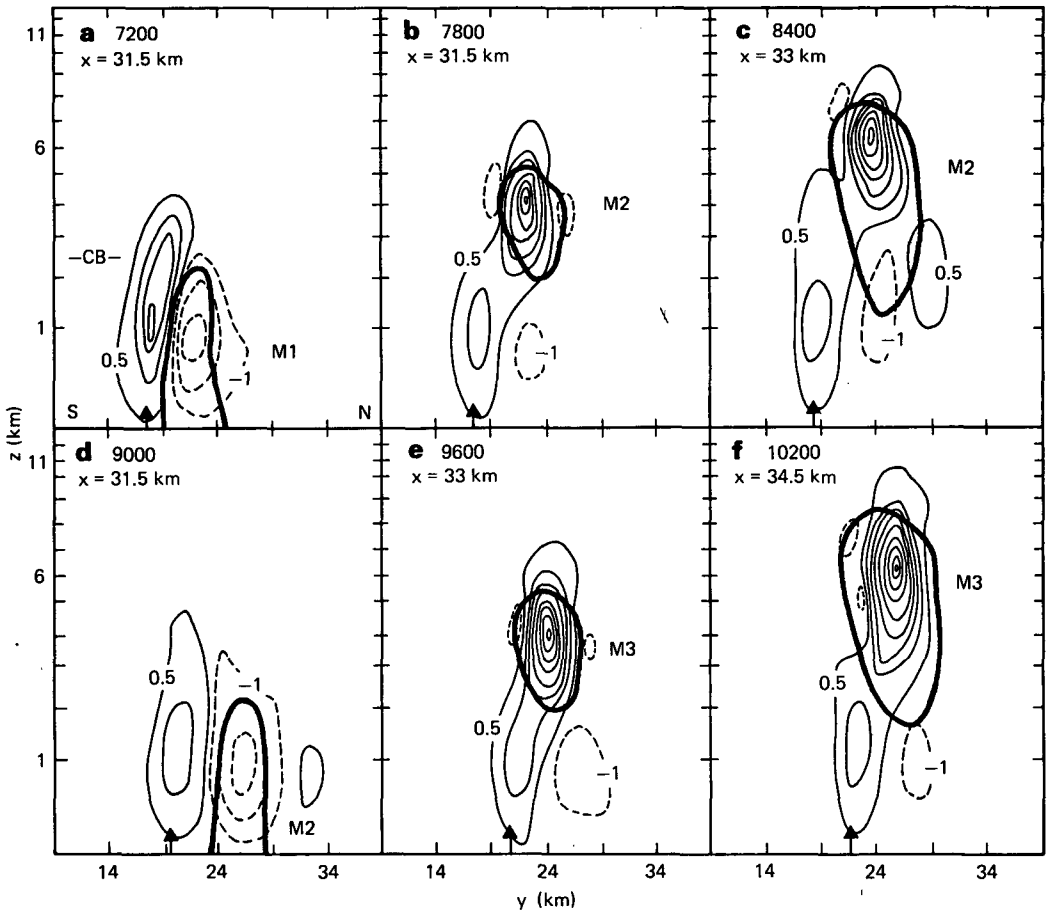

FIG. 6. The vertical velocity in north–south cross sections through the maximum vertical velocity in the model domain at the times indicated. The contour interval is 1.5 m s^{-1}. Solid lines denote positive contours starting from 0.5 m s^{-1} while dashed lines denote negative contours starting from −1 m s^{-1}. The short vertical arrows indicate the position of surface gust front. The heavy solid line encloses the region where the rain field is greater than 0.1 g kg^{-1}.

movement of the storm as a whole is toward the south-southwest at ~10 m s^{-1} (5400–13 200 s) until M5 occurs and the storm slows down. The individual cells M1–M4, however, moved to the south at ~8 m s^{-1} as illustrated in Fig. 2h and thus the generation of new cells to the southwest of preceding ones plays a part in the overall storm movement.

The development of new cells is documented further in Fig. 6 where the vertical velocity and rainwater region are shown at 10 min intervals between 2 and 3 h in north–south vertical cross sections passing through the maximum vertical velocity in the model at the times indicated. The velocity contour interval of 1.5 m s^{-1} is increased (decreased) from 0.5 m s^{-1} and the rainwater region greater than 0.1 g kg^{-1} is enclosed by the thick solid line. The distance of the vertical cross sections from the western boundary of the simulation domain is shown in the upper left corner of each panel. Only a limited portion of the north–south extent of the model domain is shown because substantial vertical motion does not exist outside this area. Further, since the integration domain is moved so that new cell development remains within it, the rain region in Fig. 6 does not appear to move to the south as shown in Fig. 5. The contours are displayed in the vertically stretched system with heights labeled to the left of the figure. In the stretched system the model resolution is greater in the boundary layer than in the cloud layer. Thus, when displayed in the stretched system clouds appear shorter than they actually are when visually contrasted with the depth of the boundary layer.

The vertical velocity and rainwater development in Fig. 6 clearly illustrate that the evolution of M3 parallels that of M2. At 7200 (9000) s, the updraft is mainly confined to the subcloud region both within the cold outflow region of M1 (M2) and within the environment to the south. This is illustrated at the

surface where the position of the cold outflow boundary indicated by the arrow divides the updraft. The cold air at 7200 (9000) s is a result of evaporation within the downdraft which at this time is in excess of 4 m s^{-1}. Without evaporation the near-surface downdraft air would have had a potential temperature close to that of the environment if all other fields remained unchanged, rather than being 6–7°C colder. The rain falling from M1 (M2) began to reach the ground ~10 min earlier. Substantial rain still exists up to ~5 km at 7200 (9000) s. Only some of this rain reaches the ground before the surface rainfall stops 5 min later because the humidity in the air below 1.2 km is less than 50% and significant evaporation occurs. The existence of rain above cloud base is not evident in the figure (panels a and d) because most of it occurs to the east of the vertical plane shown.

The growth of M2 (M3) becomes evident at 7800 (9600) s when a velocity maximum appears above cloud base and precipitation begins to form. Very little rainwater associated with M1 (M2) remains within the domain and the vertical velocities are still increasing at this time. During the following 10 min the new cells reach their maximum vertical velocities of 12 (15) m s^{-1} and tops of ~8 km. By 8400 (10 200) s rain has begun to fall below the cloud base but has not reached the ground anywhere beneath the cell. As rain continues to fall out of M2 (M3) the cell decays and a new cell M3 (M4) begins to form.

This completes another 40 min cloud life cycle. During this cycle a new cell updraft grows and rain forms within it. Over the last 15 min surface rainfall occurs. In response to the rain-induced downdraft the cold outflow air continues to move to the south where a new cell is triggered.

c. *Subcloud changes during the life cycle of cell M2*

The development of successive new cells is accompanied by periodic changes in the boundary layer. These changes are illustrated for horizontal planes in Fig. 7 at 7200, 7800, 8400 and 9000 s. In these figures only a 30 km by 30 km box is shown with distances from the southwest corner of the actual domain used in the simulation indicated. The vertical cross sections passing through the line connecting the arrows in Fig. 7a are shown in Fig. 6. The solid thick lines divide the cold outflow air from the environment air. Also, in the figures the dotted lines enclose regions in which the rainwater content is greater than 0.1 g kg^{-1}.

The cloud base vertical velocity is shown in 7a where the contour interval is 1.5 m s^{-1} and dashed lines are used in downdraft regions starting at −1.0 m s^{-1}. At 7200 s the downdraft due to M1 reaches 4.5 m s^{-1}. To the south–southwest of the downdraft region the updraft is greater than 2 m s^{-1} where cell M2 is beginning to form. To the west of this new development a weak updraft occurs in which the vertical transport of northwesterly flow relative to cell movement (shown in Fig. 4b by the solid dot) occurs. This updraft persists throughout the life cycle of M2; however, it remains shallow and no convection is initiated by it. During the 10 min period following 7200 s the updraft deepens as the cold outflow boundary moves out ahead of it in response to diverging downdraft air. At the same time the downdraft due to M1 weakens considerably. After 7800 s the M2 updraft loses its intensity as seen at 8400 s; however, rain is being produced in M2 during this time, with the associated downdraft becoming apparent at cloud base by 9000 s. The velocity patterns at this time are quite similar to those at 7200 s, and a new cycle begins.

The divergence field at 46 m associated with the updraft development at 2.6 km is shown in Fig. 7b where the contour interval is 2.5×10^{-3} s^{-1}. Strong divergence in the downdraft region is apparent at 7200 s while weaker convergence exists along the gust front. Part of this convergence region occurs within the cold air and is thus part of the gust front circulation. By 7800 s the M1 cell has rained out and the divergent region is weakening along with the 2.6 km downdraft. It does not increase again until after 8400 s when the rain induced downdraft from M2 begins to reach the ground. In contrast to the clear reflection of the downdraft in the divergence field, there is only a weak indication of the behavior of the above cloud base updraft. The small changes that occur to the south of the cold air boundary indicate enhanced convergence (either in areal coverage or magnitude) as the new updraft grows.

Systematic changes also occur in the potential temperature field at 46 m as shown in Fig. 7c where the deviation of the potential temperature is shown with a contour interval of 1.5°C. The thick contour is the cold outflow boundary located along the 0.0°C contour of the potential temperature deviation from the environmental value. At 7200 s a cold dome due to evaporation of rain in M1 is evident. This cold dome spreads out to the west and north as the downdraft decays while a relatively warm region (denoted by W) develops in the downdraft region to the east. The appearance of this warm region is accompanied by negative moisture perturbations due in part to insufficient rain in the downdraft to achieve evaporative cooling rates similar to those at 7200 s. Both the cold and warm centers then move further to the north of the gust front and a new cold center appears in the downdraft associated with M2 as seen at 9000 s.

Changes in the pressure perturbation field at 46 m are also tied strongly to the downdraft development as seen in Fig. 7d where the contour interval is 0.25 hPa (mb). Associated with the strong down-

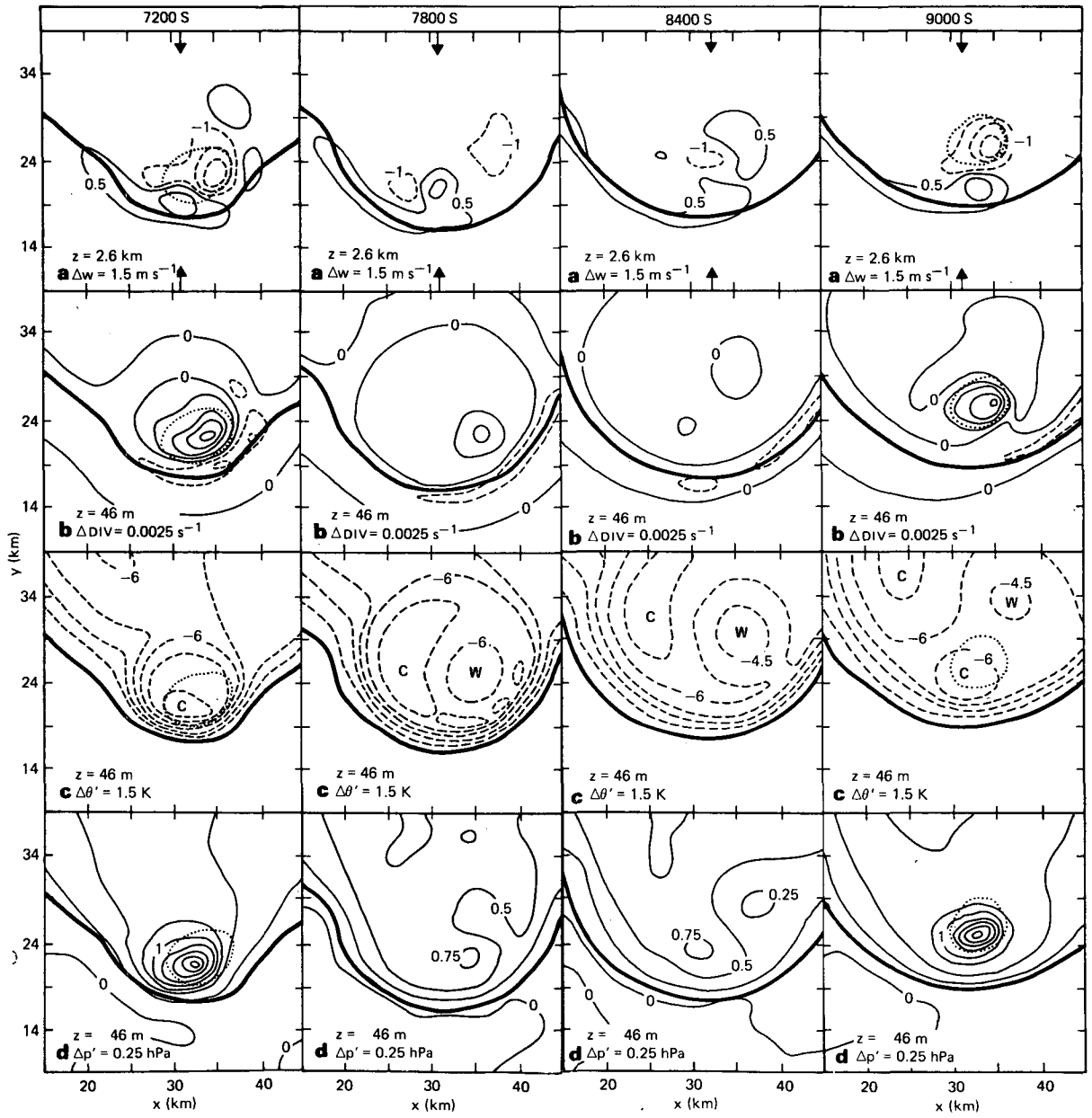

FIG. 7. Horizontal cross sections at 10 min intervals between 7200 and 9000 s. At z = 46 m the rain region greater than 0.1 g kg^{-1} is enclosed by the dotted line and the cold outflow boundary is denoted by the thick solid line. (a) The vertical velocity at z = 2.6 km AGL with a contour interval of 1.5 m s^{-1}. Solid lines denote positive contours starting from 0.5 m s^{-1} while dashed lines denote negative contours starting from −1.0 m s^{-1}. The arrows indicate the location of the vertical cross sections in Fig. 6. (b) The divergence field at z = 46 m with a contour interval of 2.5 × 10^{-3} s^{-1}. Dashed lines denote convergence while solid lines denote divergence. (c) The deviation of the potential temperature from its initial value at z = 46 m with a contour interval of 1.5°C. (d) The deviation of the pressure from its initial value at z = 46 m with a contour interval of 0.25 hPa.

draft at 7200 s is a high pressure that is ~2.0 hPa above that in the environment. This pressure decreases in time and the gradients become weaker until the new downdraft forms and it increases to ~2.0 hPa again. Thus, a significant part of the pressure variation (over 1.0 hPa) is associated with the dynamic changes near the surface.

In summary, the initial storm acts to initiate a cold region near the surface which spreads out in time. This is followed by changes near the surface which reflect the stage of development of new downdrafts and their periodic character. The changes related to the growth of new updrafts (e.g., enhanced convergence) are less pronounced, although present.

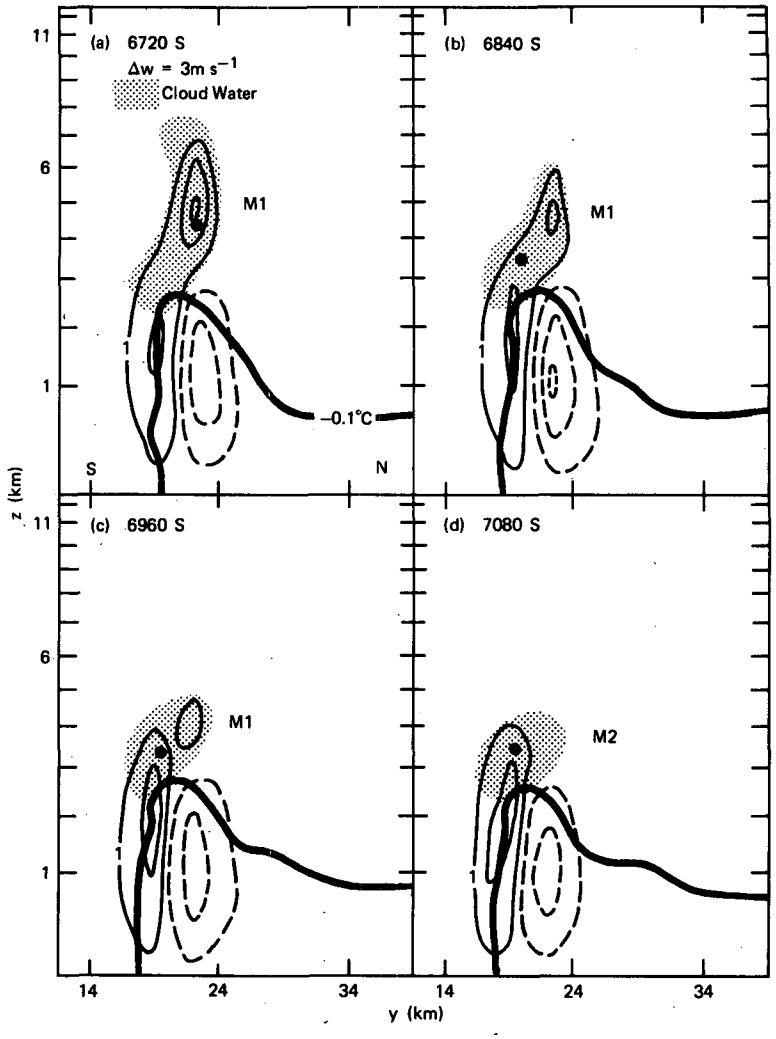

FIG. 8. Vertical cross sections at 2 min intervals and at $x = 31.5$ km passing through the decaying and newly forming updrafts associated with M1 and M2, respectively. The vertical velocity is contoured at 3 m s^{-1} intervals with solid lines in the positive region and dashed lines in the negative region. The shaded area represents cloud water in excess of 0.5 g kg^{-1} and the thick solid line is the −0.1°C contour for the deviation of the potential temperature from its original state.

d. A detailed look at new cell development

The behavior of the vertical velocity, pressure and potential temperature during the decay of M1 and the onset of M2 is explored further in this section. In Fig. 8 the development of the vertical velocity is shown at 120 s intervals beginning at 6720 s and ending at 7080 s. The vertical cross sections displayed are taken through $x = 31.5$ km, the same location as the 7200 s panel in Fig. 6a, but the 3 m s^{-1} contour interval is different. During the 6 min period shown the updraft associated with M1 decays from a peak value of 7.4 m s^{-1}. At the same time the updraft below cloud base is increasing in strength from about 4.0 to 4.8 m s^{-1} and in extent as seen by considering the region with upward motion in excess of 4 m s^{-1}. Coupled with these developments the cloud water field (shaded) associated with M1 decays and the maximum cloud water content (~1 g kg^{-1} in all panels and denoted by the dots) moves southward from inside the M1 updraft to over the updraft located primarily in the boundary layer. In response to continued condensation a new maximum in vertical velocity above the boundary layer occurs just after 7200 s along with small amounts of rain.

The relationship between the developing and decaying updraft is further illustrated at 6960 s in Fig. 9 where horizontal cross sections of vertical velocity are shown at (a) $z = 2.6$ km and (b) $z = 4.1$ km. The contour interval of 3 m s^{-1} is the same as in Fig. 8. The new updraft is apparent to the south of the old decaying one in (b). It is directly associated with

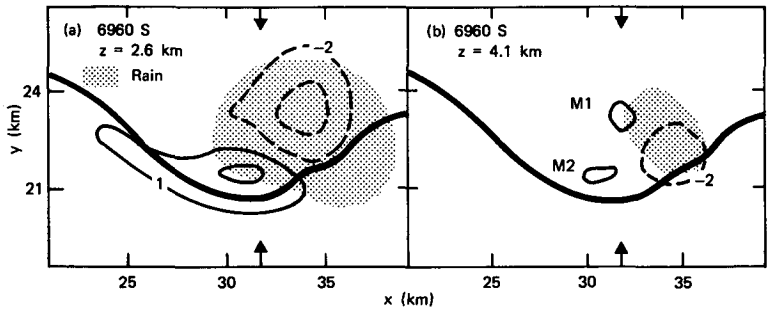

FIG. 9. Horizontal cross sections of the vertical velocity at 2.6 and 4.1 km. The contour interval is 3 m s^{-1} and the region of rain-water greater than 0.1 g kg^{-1} is densely shaded. The cold outflow boundary at z = 46 m is shown by the thick solid line. The line connecting the two arrows lies in the vertical cross sections shown in Fig. 8.

the updraft at cloud base in (a) which lies over the cold outflow boundary (thick solid line). Air in this new updraft appears to originate from 1.0 to 1.5 km above the ground, based on momentum and thermodynamic considerations. Detailed trajectory analysis is needed to confirm this, however, because the environmental boundary layer is rather well mixed thermodynamically. Also apparent in the figure is the three-dimensional character of the relationship of the updraft to the downdraft. At and below z = 2.6 km the downdraft is to the northeast of the updraft while 1.5 km higher it is to the east. At both levels it lies in the region of precipitation which is shaded.

The subcloud updraft air in Fig. 8 occurs on both sides of the line separating the evaporatively cooled downdraft air from the environmental air. The development of this line is shown in Fig. 8 by the thick contour which represents the −0.1°C perturbation in the potential temperature from its environmental state. The cold region near the leading edge extends from the cloud base to the surface and the local updraft–downdraft circulation within it is typical of outflows, i.e., rising air next to the edge and sinking further behind. However, it is worthwhile noting that the cold outflow has not proceeded far from its source in the rain-induced downdraft. Thus, the updraft–downdraft circulation is directly related to the effects of evaporative cooling in contrast to outflows with a similar circulation but which have moved substantially away from their source. The latter also develops within the model as the cold outflow propagates away from the precipitation region to the north. It is characterized by a circulation in which the updraft within the cold region is about twice the strength of the downdraft behind it, rather than being weaker as it is in Fig. 8. Further, it is confined to a shallower layer as seen in the northern part of Fig. 8.

The distribution of the potential temperature deviation from its environmental state in the cold outflow region is further documented in Fig. 10 at 6960 s when the downdraft in the boundary layer has reached its most intense stage. In response to this intense downdraft the outflow surges toward the south between 6840 and 7080 s with an increase in speed of 2 m s^{-1} (a similar increase was not found during development of M3 and M4). In the precipitation region enclosed by the thick solid line the perturbation has dipped to almost −8.4°C, the lowest value it attains during the rainout of M1. Outside this region the temperatures are somewhat warmer and to the north are ~ −5.0°C near the surface. The cold temperatures are primarily the result of evaporative cooling as previously mentioned. The evaporation of rain is sufficient to increase the moisture in descending air beyond environmental values, although the relative humidity remains below 60% in the lowest kilometer. For example, the maximum relative humidity at z = 46 m is ~51%, a value 33% greater than in the environment.

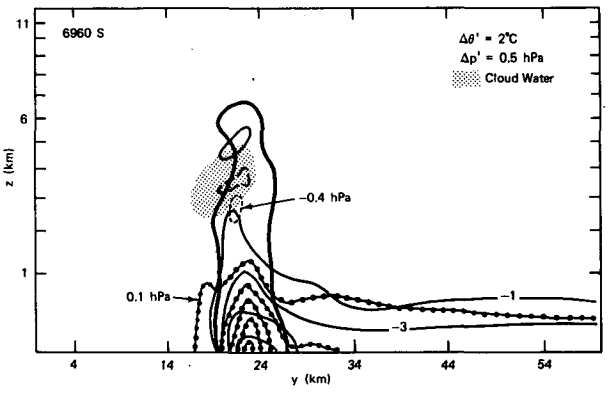

FIG. 10. A vertical cross section of the potential temperature and pressure deviations at x = 31.5 km. The potential temperature contours are dashed in positive regions and solid in negative ones and are spaced 2°C apart. The pressure deviations are displayed by dotted contours at intervals of 0.5 hPa. The region in which cloud water is greater than 0.5 g kg^{-1} is lightly shaded and the region in which rainwater is greater than 0.1 g kg^{-1} is enclosed by the thick solid line.

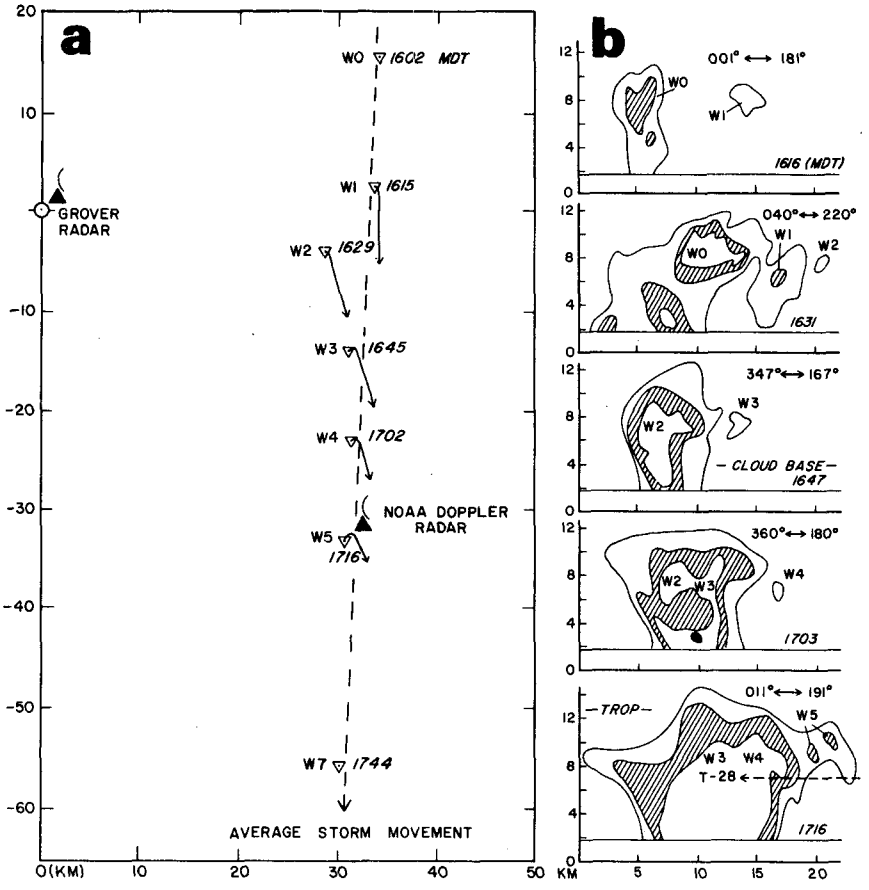

FIG. 11. (a) The inverted triangles denote the horizontal position of the first echo appearance occurring near 7 km MSL for observed cells W0 through W7. Arrows show the paths of cells W1 through W5 from first detection at the times shown to maximum reflectivity. (b) Vertical cross sections of the radar echo aligned roughly along the storm track indicated by the dashed line in (a). Reflectivity contours are in 10 dB(Z) steps starting at 30 dB(Z) (Adapted from Chalon *et al.*, 1976; Figs. 6 and 7.)

The pressure deviations at 6960 s describe a pattern similar to the potential temperature perturbations, including the occurrence of the greatest deviation within the rain region near the surface. The pressure contours are shown in Fig. 10 with dotted lines using a contour interval of 0.5 hPa (mb). The maximum surface pressure of 2.3 hPa occurs within the strong downdraft region at the time of the figure and is strongly related to the dynamics of diverging air in the downdraft. In contrast, a significant hydrostatic pressure increase is evident to the north of the rain region in response to the rather horizontally homogeneous temperature distribution in the outflow. It is also worth emphasizing that no low-pressure region occurs out ahead of the cold outflow [to the south (also see Fig. 7d)] as can occur with supercell storms (Wilhelmson and Klemp, 1981). This situation exists in part because cells do not lean to the south over the outflow boundary and alter the surface pressure hydrostatically. Further, they do not produce large amplitude gravity waves that propagate to the south.

4. Comparison of modeled and observed successive cell development

The sounding used for the model simulation discussed in the previous section was taken from observations made during the National Hail Research Program in Colorado on 9 July 1973. On this day several storm complexes occurred within the observing network. The focus of the analysis effort was directed toward examination of cellular development in the western part of the earliest echo complex. After examining the reflectivity field in this region Chalon *et al.* (1976) were able to identify five discrete echoes that formed in succession between 1602 and 1731 MDT. This development is summarized in Fig. 11a where the initial position of each echo occurring at ~7 km MSL is shown by the inverted

triangle and where the associated times shown are ~15 min apart. Each new echo appeared on radar 5–10 km to the south (M2 formed to the southwest) of the previous one and generally moved toward the south-southeast at an average speed of 4 m s^{-1} (see open circle in Fig. 4b). The overall system, however, moved to the south at ~10–12 m s^{-1}. Thus, discrete development of new cells played a major role in the propagation of the system as shown in Fig. 2g.

At any given time the system was composed of two or more cells as illustrated in Fig. 11b which shows vertical cross sections of the radar echo aligned roughly along the storm track (dashed line in Fig. 11a). The reflectivity contours start at 30 dB(Z) with increments of 10 dB(Z). Three cells are evident at all times but 1616 and 1647. New cells in the figure appear between 6 and 8 km MSL and after they have grown their echoes merge with their predecessors. The lifetime of each cell is ~45 min. This includes an estimated 15 min initial period for precipitation growth to radar detectable size. Because new cells occur at 15 min intervals a continuous echo region exists to the north of developing cells. It is interesting to note that this northern echo region appears to have been supported by a convergence region distinct from that associated with new cell formation (Fankhauser, 1976; see Figs. 7 and 8). The explanation for two distinct convergent regions is complicated by the presence of another storm complex to the east and southeast.

The development of cells in the model appears similar to the observed development in that five successive cells do form, although to the southwest rather than south of old ones as shown by the discrete propagation vectors for the observed and modeled storms in Figs. 2g and 2h, respectively. In addition, the propagation of the storm system as a whole (~10 m s^{-1} to the south) and the cell life cycles (~40 min) are similar. However, there are also many qualitative differences. The modeled cells occur every 30 min, rather than every 15 min as observed. They also move to the south almost as fast as the storm system (~8 m s^{-1}) in contrast with the slower movement of observed cells (~4 m s^{-1}) as seen by comparing cell motion vectors in Figs. 2g and 2h or in Fig. 4b. Further, the depth of the modeled cells is 3–4 km less than observed. This is reflected in the weaker modeled updrafts and downdrafts in comparison to those determined from vertically pointing Doppler radar and from aircraft measurements.

We recognize that these differences could be a result of the simplifications made in building and initializing the numerical model. The model was initiated in a horizontally homogeneous environment that was based on a sounding taken ~50 km from the observed storm development and modified with the aid of aircraft data. Based on this sounding the model was integrated for 4 h with marginal horizontal resolution for resolving the cells with dimensions of 5–10 km and with highly parameterized warm rain microphysics. Mesoscale variability and convergence were not included and no attempt was made to represent the effects of another storm just to the east of the one studied and whose development does not appear to be characterized by successive cell development. It is also possible that terrain features may have had some effect on the observed storm development, although such effects were not modeled.

One difference between the modeled and observed storm development will be discussed further because it illustrates the complexity of observed events and how this influences overall storm behavior. The average speed of the observed cells was ~4 m s^{-1} to the south as shown by the open circle in Fig. 4b. In contrast, the speed of the modeled cells (solid circle) is about twice as fast. The modeled cell speed is within 2 m s^{-1} of the average environmental wind vector between the surface and 6.5 km MSL represented by the plus sign in Fig. 4b or of the mean between the surface and the 9.5 km represented by the triangle. The observed cells, however, move at a slower speed than all the environmental wind vectors between 2.3 and 10 km MSL.

This slow speed has several possible interpretations. One is that the observed cell speeds were governed by the flow in the lowest kilometer, i.e., by flow at least 1 km below cloud base. It is possible to use conservation of updraft momentum to make this argument; however, other factors such as the influence of downdraft momentum and of entrainment would also be important. Further, Fankhauser and Mohr (1977) indicate that cell speeds in weakly and strongly organized multicellular complexes do not typically move in the direction of or with the speed of the lowest kilometer winds. Another interpretation is that the environmental wind profile (STK, 1630) shown in Fig. 4b and used in the model simulation is not entirely representative of the environment in which the multicells occurred. It is worthwhile noting that several other available wind profiles are similar to the one shown in Fig. 4b (Grover at 1735, and Kimball at 1725). However, all the soundings were at some distance from the storm complex and it is possible that the storm motion could have been influenced by alternations in the wind profile due to the other storm just to the east or to previous cells to the north. For example, the eastern storm and northern cells could have blocked environmental flow from the north at all levels between 2.5 and 10 km with respect to observed individual cell movement. Blocking of flow by a cloud mass and reduction in wind speeds can occur as well illustrated by Klemp *et al.* (1981; Figs. 4c and 4d) for a modeled supercell storm and as discussed by Hoxit *et al.* (1976) based on observations. However, this did not occur on a

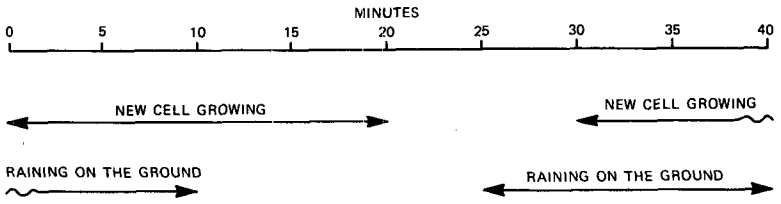

FIG. 12. A time line showing the relation between the development of a modeled cell and the cells before and after it.

sufficiently large enough scale in the model simulation. In part, this is because the storm mass was only the size of an individual cell rather than of several cells together and because the effects of the eastern storm were not included. Thus, the horizontal variability in winds could have played an important role in determining the details of the observed successive cell development.

Despite the simplifications made in modeling the observed storms and the differences that result, we believe that continued model experimentation will produce a better understanding of the nature of successive cell development. With regard to the simulation, it is encouraging that successive cells can be modeled. The reasons for the difference in the period of new cell development (every 30 min as modeled and every 15 min as observed) remain unclear. However, it is worth recalling that periods similar to the one modeled have been observed (e.g., see Fig. 3).

5. Conclusions

The propagation of storms can be significantly affected by the successive generation of new cells as amply documented in the literature since the paper by Brooks (1946). The development of these new cells can occur periodically with intervals as small as 10 min and as large as 30 min. The implications of discrete propagation associated with both periodic and irregular new development have been illustrated in Fig. 2 for a number of observed multicell storms. The magnitude of the discrete propagation vectors should be tied to the frequency of new cell formation (when it is regular) to determine how far away from the main storm system that new cells will form. This is less than 10 km in all the cases illustrated except that shown in Fig. 2f.

In this paper we have discussed a numerical simulation in which five new cells formed in succession over 4 h. Each of these cells existed for ~40 min as illustrated in Fig. 12. The time line in this figure originates at the start of formation of a cell. The updraft in this cell grows in strength for ~20 min. About 5 min later, the rain generated within it reaches the ground. This is followed by the formation of a new updraft 30 min after the original cell was triggered. New cell development causes the storm complex to move to the right of individual cell movement (Fig. 2h) as commonly observed in multicell storms. The period of new development is ~30 min, slightly greater than for one multicell storm discussed in the Introduction (see Fig. 3).

The development of both modeled (including that reported here) and observed cells typically occurs over or just behind the cold outflow boundary set up by previous cells. Air approaching the outflow boundary is either diverted around the cold region or rises up and over it. If this air rises over the top of the cold region it can trigger new cell development, help to supply an existing updraft with moist low-level air, or continue to move over the cold region without setting off any new convection. Weisman and Klemp (1982) and Wilhelmson and Chen (1982) have shown that the strength and distribution of the vertical shear of the environmental wind is an important factor in determining what air rising over an expanding cold outflow will do. For example, in strong low to mid-level shear, supercell storms with long lifetimes can occur. In somewhat weaker shears successive short-lived cells will develop.

In the model simulation new cell generation occurs ~5 min after the most recent cell produces surface precipitation (see Fig. 12) and so it appears that new cell generation is tied to outflow enhancement due to this downdraft. However, from other simulations the separation speed between old cells and the outflow seems to be a more general controlling factor on the timing of new cell generation because it can be used to explain more frequent development of new cells. Precipitation-induced downdrafts then act primarily to sustain the outflow and their timing is not directly related to the timing of new cell formation. We are continuing to investigate the factors that control the period and location of new cell development.

Acknowledgments. The authors wish to thank Ms. K. Garrelts for typing the manuscript and Mr. Kelvin Droegemeier for his comments on it. The model simulation was performed on the CRAY-1 computer at the National Center for Atmospheric Research which is supported by the National Science Foun-

dation. This work was supported by the National Science Foundation under NSF Grants ATM 78-01010 and ATM 80-11984.

APPENDIX

Additional Details of the Numerical Cloud Model

The numerical cloud model used to obtain the results in this paper was based on the one developed by Klemp and Wilhelmson (1978a). An overall view of the changes made in the model is given in Section 2. Some of these changes are more fully documented in this Appendix.

One of the changes made to the model was the incorporation of a vertically stretched grid obtained by continuously mapping the actual vertical coordinate z in domain D into the coordinate z' in domain D'. The equation defining this transformation is the same as the one used by Anthes (1970) and is

$$z = (C_1 + C_2 z')z'. \tag{1}$$

A constant grid interval $\Delta z'$ is used in the z' coordinate system so that the actual height of a grid point can be determined from

$$z = (C_1 + C_2 z_1')z_1', \tag{2}$$

$$z' = \begin{cases} I\Delta z' & (I = 0, 1, \ldots, NT) \\ & \text{for the vertical velocity} \\ (I - 1/2)\Delta z' & (I = 1, 2, \ldots, NT) \\ & \text{for all other variables.} \end{cases}$$

Here $NT \cdot \Delta z'$ is the depth of the domain and the grid is staggered. If the height of any level and the height of the domain are known, then C_1 and C_2 can be determined using NT and $\Delta z'$. The mapping factor M is defined as

$$M \equiv \frac{dz'}{dz} = \frac{1}{C_1 + 2C_2 z'}. \tag{3}$$

Using this definition the vertical derivative $\partial F/\partial z$ of any function F in z coordinates can be transformed into z' coordinates by

$$\frac{\partial F}{\partial z} = M \frac{\partial F}{\partial z'}. \tag{4}$$

Similarly, the second derivative of F can be transformed using

$$\frac{\partial^2 F}{\partial z^2} = M \frac{\partial}{\partial z'}\left(M \frac{\partial F}{\partial z'}\right). \tag{5}$$

These transformations were applied to the equations given by Klemp and Wilhelmson using NT = 26, $\Delta z' = 500$ m, $C_1 = 0.168$ and $C_2 = 6.4 \times 10^{-5}$ m^{-1}. Cloud base occurs at about 2.6 km AGL in the reported simulation and thus the resolution in the boundary layer ranges from 100 to 400 m while above it ranges from 400 to 900 m.

Another change was made to the Klemp-Wilhelmson model to improve the conservation associated with advection while retaining fourth-order accuracy in the horizontal. The equations for velocities and for mixing ratios of water vapor, cloud water and rainwater were written in flux form, i.e.,

$$\phi_t = -u\phi_x - v\phi_y - wM\phi_{z'} = -(u\phi)_x - (v\phi)_y - M(\bar{\rho}w\phi)_{z'}\bar{\rho}^{-1} + \phi[u_x + v_y + M(\bar{\rho}w)_{z'}]. \tag{6}$$

Here ϕ is the quantity being advected and $\bar{\rho}$ the base state density which is only a function of z'. A conservative fourth-order, nonlinear approximation was then devised for the horizontal fluxes with the aid of Taylor series expansions. The vertical flux term was approximated using second-order centered differences. With the aid of the standard operators

$$\delta_{nx}\phi(x_j) \equiv \frac{1}{n\Delta x}[\phi(x_j + n\Delta x/2) - \phi(x_j - n\Delta x/2)],$$

$$\overline{\phi(x_j)}^{n\Delta x} \equiv \frac{1}{2}[\phi(x_j + n\Delta x/2) + \phi(x_j - n\Delta x/2)],$$

the finite difference flux forms for the velocities u, v and w at their respective staggered grid locations are

$$(uu)_x + (uv)_y + M(\bar{\rho}wu)_{z'}\bar{\rho}^{-1} \approx \frac{10}{8}\delta_x(\bar{u}^x\bar{u}^x) - \frac{1}{8}\delta_x(\bar{u}^{3x}\bar{u}^{3x}) - \frac{1}{8}\delta_{3x}(\bar{u}^x\bar{u}^x) + \frac{10}{8}\delta_y(\bar{v}^x\bar{u}^y) - \frac{1}{8}\delta_y(\bar{v}^x\bar{u}^{3y}) - \frac{1}{8}\delta_{3y}(\bar{v}^{3x}\bar{u}^y) + M\delta_z(\overline{\bar{\rho}^{z'}w\,\bar{u}^{z'}}^x)/\bar{\rho}, \tag{7}$$

$$(uv)_x + (vv)_y + M(\bar{\rho}wv)_{z'}\bar{\rho}^{-1} \approx \frac{10}{8}\delta_x(\bar{u}^y\bar{v}^x) - \frac{1}{8}\delta_x(\bar{u}^y\bar{v}^{3x}) - \frac{1}{8}\delta_{3x}(\bar{u}^{3y}\bar{v}^x) + \frac{10}{8}\delta_y(\bar{v}^y\bar{v}^y) - \frac{1}{8}\delta_y(\bar{v}^{3y}\bar{v}^{3y}) - \frac{1}{8}\delta_{3y}(\bar{v}^y\bar{v}^y) + M\delta_z(\overline{\bar{\rho}^{z'}w\,\bar{v}^{z'}}^y)/\bar{\rho}, \tag{8}$$

$$(uw)_x + (vw)_y + M(\bar{\rho}ww)_{z'}\rho^{-1} \approx \frac{10}{8}\delta_x(\bar{u}^{z'}\bar{w}^x) - \frac{1}{8}\delta_x(\bar{u}^{z'}\bar{w}^{3x}) - \frac{1}{8}\delta_{3x}(\bar{u}^{3z'}\bar{w}^x) + \frac{10}{8}\delta_y(\bar{v}^{z'}\bar{w}^y) - \frac{1}{8}\delta_y(\bar{v}^{z'}\bar{w}^{3y}) - \frac{1}{8}\delta_{3y}(\bar{v}^{3z'}\bar{w}^y) + M\delta_z(\overline{\bar{\rho}^{z'}w\,\bar{w}^{z'}}^{z'})/\bar{\rho}^{z'}. \tag{9}$$

The flux approximations for the mixing ratio of water vapor, cloud water, rainwater and mixing coeffi-

cients, all defined at the same point and represented by ϕ, are

$$(u\phi)_x + (v\phi)_y + M(\bar{\rho}w\phi)_z\bar{\rho}^{-1} \approx \frac{10}{8}\delta_x(u\bar{\phi}^x) - \frac{1}{8}\delta_x(u\bar{\phi}^{3x}) - \frac{1}{8}\delta_{3x}(u\bar{\phi}^x) + \frac{10}{8}\delta_y(v\bar{\phi}^y) - \frac{1}{8}\delta_y(v\bar{\phi}^{3y}) - \frac{1}{8}\delta_{3y}(v\bar{\phi}^y) + M\delta_z(\bar{\rho}^z w\bar{\phi}^z)\bar{\rho}^{-1}. \quad (10)$$

The potential temperature, however, is still predicted using the advective form given by Klemp and Wilhelmson (1978a) since in flux form it is not independent from the pressure equation.

The bracketed term in (6) is zero in anelastic (incompressible) systems such as those used by Wilhelmson (1974) and Schlesinger (1975). In the simulation reported in this paper this term is also considered to be zero since the desired solution is the anelastic one. Sound waves are still represented in the model when this is done and thus the computational advantages discussed by Klemp and Wilhelmson (1978a) still pertain. Further, density ($\bar{\rho}$) weighted quantities such as water vapor are conserved in the integration domain apart from phase changes and fluxes through the boundaries. We recognize that ignoring the bracketed term is an approximation to the earlier system of equations used. That system was also formed on the basis of a number of approximations. We compared solutions obtained using the bracketed term with those in which it is not used and found the solutions to be quite similar for periods of an hour or two and qualitatively similar thereafter. It is not possible to say with certainty, however, which solution is the better one since both systems are approximate ones. However, the approach used in this paper did lead to improved conservation based on some two-dimensional comparisons presented by Chen (1980).

Since the numerical model is integrated over a limited domain, some kind of lateral boundary condition must be applied which will allow disturbances occurring inside the domain to propagate out of the domain. Orlanski (1976) proposed an extrapolation scheme in which each dependent variable of the solution is determined by its own "phase velocity". Klemp and Lilly (1978) used a similar extrapolation scheme, but in which the phase velocity was estimated before the simulation, rather than computed during it. Further, this extrapolation was used only in determining the normal velocity at the boundaries and was adopted by Klemp and Wilhelmson (1978a) in their three-dimensional cloud model. Klemp and Wilhelmson further specified the normal derivative of all variables except the normal velocity to be zero at inflow points along lateral boundaries (normal velocity directed into the domain). At outflow points normal derivatives were calculated using upstream differencing.

In the simulation reported in this paper the specification of boundary conditions is the same as used by Klemp and Wilhelmson (1978a) except that the "phase velocity" is computed in a manner similar to Orlanski (1976). In this way the phase velocity is determined by the evolving solution and does not depend on a prior decision. This is convenient because a bad *a priori* choice can lead to undesirable results. For example, in some of his simulations Clark (1979) chose a rather large fixed phase velocity which probably led to continual growth in the mean vertical motion within his model domain. The use of a changing phase velocity in this paper does not imply that the solution will be better than that obtained with a fixed velocity since both approaches are only approximate attempts to allow a variety of waves to leave the model domain. It is our philosophy that whenever possible, results from a specific case study should be checked by increasing the domain size while holding the grid resolution constant. The simulation reported in this paper was done with a large domain. Comparisons with smaller domain simulations and different boundary treatments are described in Chen (1980). In addition, the horizontal average of vertical motion did not grow in time and remained below 0.1 m s^{-1} in absolute value at all levels.

The computation of the phase velocity differs from that given by Orlanski (1976) in that it is calculated with two rather than three time levels for computational reasons. This can be illustrated for the normal velocity u at $x = 0$, the left boundary. The radiation equation that is approximated there is

$$u_t = -c^*u_x = -(u - c^{**})u_x, \quad (11)$$

where c^* is computed at each boundary point every time step in contrast to the *a priori* specification of c^{**} used by Klemp and Wilhelmson (1978a). The finite difference equation for the determination of c^* at time $n + 1$ is the forward-time, upstream space approximation given by

$$c^* = -\Delta x(u^n_{\Delta x} - u^{n-1}_{\Delta x})/[\Delta t(u^{n-1}_{2\Delta x} - u^{n-1}_{\Delta x})]. \quad (12)$$

If $-\Delta x/\Delta t \leq c^* \leq 0$, c^* is used to compute the new u^{n+1} with a similar stable approximation given by

$$u^{n+1}_0 = u^n_0 - c^*(u^n_{\Delta x} - u^n_0)\Delta t/\Delta x. \quad (13)$$

If c^* does not lie in this range it is taken to be zero. With this approach a single wave can be transmitted through the boundary with no reflection as in Orlanski's formulation.

REFERENCES

Anthes, R. A., 1970: Numerical experiments with a two-dimensional horizontal variable grid. *Mon. Wea. Rev.*, **98**, 810–822.

Brooks, H. B., 1946: A summary of some radar thunderstorm observations. *Bull. Amer. Meteor. Soc.*, **27,** 557–563.

Browning, K. A., 1962: Cellular structure of convective storms. *Meteor. Mag.*, **91,** 341–350.

——, 1977: The structure and mechanism of hail storms. *Meteor. Monogr.*, No. 38, Amer. Meteor. Soc., 1–39.

——, and F. H. Ludlam, 1960: Radar analysis of a hailstorm. Tech. Note No. 5, Dept. of Meteorology, Imperial College, London, 106 pp.

Chalon, J.-P., J. C. Fankhauser and P. J. Eccles, 1976: Structure of an evolving hailstorm. Part I: General characteristic and cellular structure. *Mon. Wea. Rev.*, **104,** 564–575.

Chen, C. S., 1980: The effect of the gust front on the generation of new convection. Ph.D. thesis, University of Illinois.

Chisholm, A. J., 1973: Radar case studies and airflow models. *Alberta Hailstorms, Meteor. Monogr.*, No. 26, Amer. Meteor. Soc., 1–36.

——, and J. H. Renick, 1972: The kinematics of multicell and supercell Alberta hailstorms. Alberta Hail Studies 1972, Research Council of Alberta, Hail Studies Report No. 72-2, 24-31.

Clark, T. L., 1979: Numerical simulations with a three-dimensional cloud model: Lateral boundary condition experiments and multicellular severe storm simulations. *J. Atmos. Sci.*, **36,** 2191–2215.

Fankhauser, J. C., 1976: Structure of an evolving hailstorm. Part II: Thermodynamic structure and airflow in the near environment. *Mon. Wea. Rev.*, **104,** 576–587.

——, 1982: *Hail Storms of the Central High Plains*, Vol. 2, Part I: 22 June 1976 case study—a complex multicellular hail and rainstorm. Chap. 13: Large-scale influences, radar echo structure and mesoscale circulations, C. Knight, P. Squires, Eds., Colorado Assoc. University Press.

——, and C. G. Mohr, 1977: Some correlation between various sounding parameters and hailstorm characteristics in northeast Colorado. *Preprints 10th Conf. Severe Local Storms,* Omaha, Amer. Meteor. Soc., 218–225.

Hoxit, L. R., C. F. Chappell and J. M. Fritsch, 1976: Formation of mesolows or pressure troughs in advance of cumulonimbus clouds. *Mon. Wea. Rev.*, **104,** 1419–1428.

Kessler, E., 1969: *On the Distribution and Continuity of Water Substance in Atmospheric Circulation. Meteor. Monogr.*, No. 32, Amer. Meteor. Soc., 84 pp.

Klemp, J. B., and D. K. Lilly, 1978: Numerical simulation of hydrostatic mountain waves. *J. Atmos. Sci.*, **35,** 78–107.

——, and R. Wilhelmson, 1978a: The simulation of three-dimensional convective storm dynamics. *J. Atmos. Sci.*, **35,** 1070–1096.

——, and ——, 1978b: Simulations of right and left moving storms through storm splitting. *J. Atmos. Sci.*, **35,** 1097–1110.

——, —— and P. S. Ray, 1981: Observed and numerically simulated structure of a mature supercell thunderstorm. *J. Atmos. Sci.*, **38,** 1558–1580.

Marwitz, J. D., 1972: The structure and motion of severe hailstorms. Part II: Multi-cell storm. *J. Appl. Meteor.*, **11,** 180–188.

Miller, M. J., 1978: The Hampstead storm: A numerical simulation of a quasi-stationary cumulonimbus system. *Quart. J. Roy. Meteor. Soc.*, **104,** 351–365.

Mitchell, K. E., and J. B. Hovermale, 1977: A numerical investigation of the severe thunderstorm gust front. *Mon. Wea. Rev.*, **105,** 657–675.

Musil, D. J., E. L. May, P. L. Smith, Jr. and W. R. Sand, 1976: Structure of an evolving hailstorm. Part IV: Internal structure from penetrating aircraft. *Mon. Wea. Rev.*, **104,** 596–602.

Newton, C. W., and J. C. Fankhauser, 1975: Movement and propagation of multicellular convective storms. *Pure Appl. Geophys.*, **113,** 747–764.

Orlanski, I., 1976: A simple boundary condition for unbounded hyperbolic flows. *J. Comput. Phys.*, **21,** 251–269.

Ray, P. S., B. C. Johnson, K. W. Johnson, J. S. Bradberry, J. J. Stephens, K. K. Wagner, R. B. Wilhelmson and J. B. Klemp, 1981: The morphology of several tornadic storms on 20 May 1977. *J. Atmos. Sci.*, **38,** 1643–1663.

Schlesinger, R. E., 1975: A three-dimensional numerical model of an isolated deep convective cloud: Preliminary results. *J. Atmos. Sci.*, **32,** 934–957.

Thorpe, A. J., and M. J. Miller, 1978: Numerical simulations showing the role of the downdraft in cumulonimbus motion and splitting. *Quart. J. Roy. Meteor. Soc.*, **104,** 873–893.

Tripoli, G. J., and W. R. Cotton, 1980: A numerical investigation of several factors contributing to the observed variable intensity of deep convection over South Florida. *J. Appl. Meteor.*, **19,** 1037–1063.

Weisman, J. L., and J. B. Klemp, 1982: The dependence of numerically simulated convective storms on vertical wind shear and buoyancy. *Mon. Wea. Rev.*, **110,** 504–520.

Wilhelmson, R. B., 1974: The life cycle of a thunderstorm in three dimensions. *J. Atmos. Sci.*, **31,** 1629–1651.

——, and J. B. Klemp, 1978: A numerical study of storm splitting that leads to long-lived storms. *J. Atmos. Sci.*, **35,** 1975–1986.

——, and ——, 1981: A three-dimensional simulation of splitting severe storms on 3 April 1964. *J. Atmos. Sci.*, **38,** 1581–1600.

——, and Chen, C. S., 1982: Cell development along cold outflow boundaries. *Preprints 12th Conf. Severe Local Storms,* San Antonio, Amer. Meteor. Soc., 127–130.